Study of Test Time Extension in KAIST Shock Tunnel

Journal of Propulsion and Energy Vol. 1, No. 1. October 2020; 1(1): 11-23
https://doi.org/10.6108/JPNE.2020.1.1.011
pISSN 2734-1887 eISSN 2765-0049

JPNE

Study of Test Time Extension in KAIST Shock Tunnel

Keunyeong Kim [a] · **Gisu Park** [b,*]

[a] Graduate Student, Department of Aerospace Engineering, Korea Advanced Institute of Science and Technology, Daejeon 34141, Korea
[b] Associate Professor, Department of Aerospace Engineering, Korea Advanced Institute of Science and Technology, Daejeon 34141, Korea

Corresponding author *
Gisu Park
gisu82@kaist.ac.kr

Received : 19 March 2020
Revised : 28 June 2020
Accepted : 2 July 2020

Shock tunnels have been used to simulate and study high-speed flow conditions; however, they usually provide a short duration of test time, which is less than milliseconds. In this study, the driver gas tailoring technique was used to extend the shock tunnel test time. The flow and the wave behavior inside the shock tube were summarized. The calculation processes of the tailored driver gas compositions were presented. The filling conditions of the driver tube corresponding to the tailored driver gas compositions were calculated. The test time extension was examined through the measurements of pressure behind the reflected shock wave near the shock tube end wall and pitot pressure at the nozzle exit.

Key Words: Shock tunnel, Driver gas tailoring, Reflected shock wave, Contact surface

Nomenclature

a	Acoustic speed, m/s
C_P	Specific heat at constant pressure, J/(kg·K)
C_V	Specific heat at constant volume, J/(kg·K)
ε	Relative difference, %
h	Enthalpy, J/kg
M	Mach number, dimensionless
P	Pressure, Pa
T	Temperature, K
t	Time, s
v	Velocity, m/s
X	Mole fraction, dimensionless
x	Position, m
γ	Specific heat ratio, dimensionless
ρ	Density, kg/m^3
$\mathcal{M}$	Molecular weight, kg/mol

Subscript	
b	Base gas
m	Mixing gas
pt	Pitot
R	Reflected shock wave
S	Incident shock wave
$Tailored$	Tailored condition
0	Total
1	Filling condition of driven gas (test gas)
2	Flow condition behind incident shock wave
3	Flow condition behind contact surface
4	Filling condition of driver gas
5	Flow condition behind reflected shock wave
8	Flow condition behind contact surface after interaction
∞	Freestream

1. Introduction

Various types of ground test facilities have been used to study high-speed flow phenomena [1]. Physical properties such as flight Mach number, Reynolds number, freestream temperature, and total enthalpy should be simulated to conduct experimental studies of the high-speed flow phenomena using ground test facilities. Impulse facilities, represented by shock tubes and shock tunnels, generate a high-enthalpy flow with high Mach and Reynolds numbers through a strong incident shock wave generation. Compared to other facilities, such impulse facilities can simulate a wide range of high-temperature flows and have the advantage of simplicity in construction and operation.

Over the years, experimental and numerical studies of high-speed flow phenomena have been conducted using the shock tube and the shock tunnel at Korea Advanced Institute of Science and Technology (KAIST) [2-15]. Table 1 summarizes the representative studies. Only the test conditions in which pressure measurements were taken are summarized in the table. Facility/Mode in the table represents a used KAIST impulse facility and its mode (shock tube or shock tunnel). The test flow conditions in the references are represented by the total flow enthalpies of test flow. Test times in the table are the examined steady flow time based on pressure measurements near the end wall (for shock tube) or the nozzle exit (for shock tunnel).

Using the 9 m impulse facility (referred to as K1 in the table), which can be used for both the shock tube and the shock tunnel modes, studies in various fields, such as gas/surface interaction, spectroscopy, and high-altitude simulations, have been conducted. The test times were significantly affected by the total flow enthalpies of test flow and the test gas compositions. For the high-enthalpy test flow with shock tube mode, the test times with tens microseconds were obtained. Because of the short-duration test times, the limits were usually given to the sampling of spectroscopy and heat flux measurements. The shock tunnel experiments were conducted under relatively low-enthalpy flow conditions, and the longer test times were obtained.

The 19 m shock tunnel referred to as K2 in the table had been used to study flameholding characteristics of the model scramjet. In the early experiments, test time was examined as about a few hundreds of microseconds based on the pitot pressure history of the nozzle exit flow [12]. One of the main reasons was that the initial driven tube length-to-diameter ratio of the K2 facility was small. Therefore, the driver and the driven tubes were made longer to extend the test time [16]. Test time of 3000 microseconds was then obtained. However, high cost was paid for the elongations, and the helium consumption rate was increased due to the enlarged volume of the driver tube. An efficient method was required for the test time extension of the KAIST impulse facilities.

For conventional reflected-shock tubes or shock tunnels, the following factors prevent the formation of uniform test flows: 1) incident shock wave attenuation [17,18]; 2) flow disruption generating from contact surface/ reflected shock wave interaction [19]; and 3) expansion wave arrival [20, 21]. Analytic and experimental studies have been

Table 1. Summary of test conditions and test time of KAIST impulse facilities.

Ref.	Facility/Mode	Facility length [m]	Year	Test condition [MJ/kg]	Driver/Test gases	Test time [μs]
2	K1/tube	4.3	2013	1.92, 2.66, 4.24	He/O2-Ar	70, 55, 45
3	K1/tube	4.3	2016	2.01, 4.41, 5.76	He/N2-Kr	75, 40, 18
4	K1/tube	4.3	2019	6.13	He/Air	90
5-7	K1/tube	4.3	2019	4.23	He/O2-Ar	10
8	K1/tube	4.3	2020	5.2	He/N2-Ar	25
9	K1/tunnel	8.7	2017	1.65	He/Air	500
10	K1/tunnel	8.7	2017	1.34	He/Air	600
11	K1/tunnel	8.7	2017	1.60	He/Air	600
12	K2/tunnel	12.8	2015	1.47	He/Air	290
13	K2/tunnel	12.8	2016	1.47	He/Air	310
14	K2/tunnel	12.8	2018	1.06, 1.39, 1.72	He/Air	800, 700, 620
15	K2/tunnel	19.3	2019	1.57	He/Air	3000

conducted to extend the test time of impulse facilities by eliminating or minimizing these factors.

The contact surface tailoring technique, which controls the interaction between the contact surface and the reflected shock wave to minimize pressure increase or decrease, is known to extend the steady period by slightly altering the physical properties of the driver or the test gas [22-25]. Various gas mixtures have been used as the test gas to satisfy the tailoring conditions within the incident shock wave Mach number range of 3.3 to 4.5 [26]. However, the test conditions are changed when the test gas properties are adjusted to satisfy the tailoring conditions. Therefore, the driver gas properties are usually adjusted to satisfy the contact surface tailoring conditions, which is known as driver gas tailoring. Using CO_2-He and C_3H_8-He mixtures as the driver gas, Amadio et al. [24] showed that the shock tube test time could be extended from 1 ms to 15 ms at low-to-intermediate temperatures. A theoretical model was developed to calculate the tailored driver gas compositions for a convergent shock tube with a driver tube that has a larger diameter than the driven tube. This model was then verified using the experimental results conducted in the Stanford high-pressure shock tube facility [25]. The various test time extension strategies of shock tubes were summarized in Reference [21].

In this study, the driver gas tailoring technique was used to extend the test time of the K1 (KAIST 1) shock tunnel. The tailored mole fraction curves of the commonly used driver gases were calculated using shock tube flow modeling with a uniform diameter. The filling pressure corresponding to the modified driver gas composition was calculated to recover the incident shock wave Mach number. The effect of driver gas tailoring was examined by measuring the pressure near the shock tube end wall and at the nozzle exit.

2. Methods and Approach

2.1 Background

A shock tunnel is a type of impulse facility equipped with a nozzle and a test section at the end wall of the shock tube. The flow behavior inside the shock tube must be examined to extend the shock tunnel test time. In the case of a simple conventional driven shock tube, the flow and waves behave like Fig. 1. The driver tube and the driven tube were initially charged with the driver and test gases,

respectively. A strong incident shock wave was generated because of the high-pressure difference across these two gases at t=0. The incident shock wave propagated to the shock tube end wall. The flow conditions of the initial test and driver gases are referred to herein as conditions (1) and (4), respectively. The flow condition behind the incident shock wave is referred to herein as condition (2). The contact surface, which is the interface of the driver and the test gases, propagated along the back of the incident shock wave. Flow condition (3) designates the flow behind the contact surface. When the incident shock wave reached the end wall, the shock wave reflected against the flow. The test gas was compressed to high pressure and temperature by the incident and reflected shock wave propagation. This flow condition is referred to herein as condition (5). The idealized test periods for the shock tube began when the incident shock wave arrived at the shock tube end wall. The compressed gas expanded through the converging-diverging nozzle and reached the test section. The test time for the shock tunnel tests began after the developments of the nozzle exit flow. Meanwhile, the reflected shock wave interacted with the followed contact surface. The wave behavior after the interaction was determined by the flow conditions, such as pressure, acoustic speeds, and molecular weight, of the flow behind the reflected shock wave and the flow behind the contact surface.

Figure 2 shows three different wave behaviors after the contact surface/reflected shock wave interaction. The x-t diagrams of Fig. 2 focus on the shock tube end wall before and after the interaction. In the figure, condition (8) represents the flow condition behind the contact surface after the interaction. If, as shown in Fig. 2a, the pressure of conditions (5) and (8) was the same, the contact surface was in the near-stationary state after the interaction, and no compression or expansion waves were generated. If the pressure of condition (5) was smaller than that of condition (8), the contact surface slowly propagated to the shock tube end wall after the interaction, as shown in Fig. 2b. Some portions of the reflected shock wave would also be reflected from the interface, resulting in the generation of multiple compression waves. The test flow pressure (same as in condition (5)) gradually increased owing to the arrival of the compression waves. Conversely, if the pressure of condition (5) was greater than that of condition (8), the contact surface would move away from the shock tube end wall after the interaction, as shown in Fig. 2c. Multiple expansion waves would then be generated at the interface. The test flow pressure gradually decreased when the expansion wave reaches the end wall. The conditions corresponding to each case are called tailored, over-tailored, and under-tailored conditions. For the shock tube satisfying the tailoring conditions, the test flow conditions were maintained for a relatively long period compared to the other two cases because no pressure disturbance was generated at the interface of the contact surface/reflected shock wave interaction. The contact surface tailoring condition could be satisfied by adjusting the properties of the driver or test gases. The test gas properties are directly related to the test flow condition; hence, the driver gas properties should be adjusted to

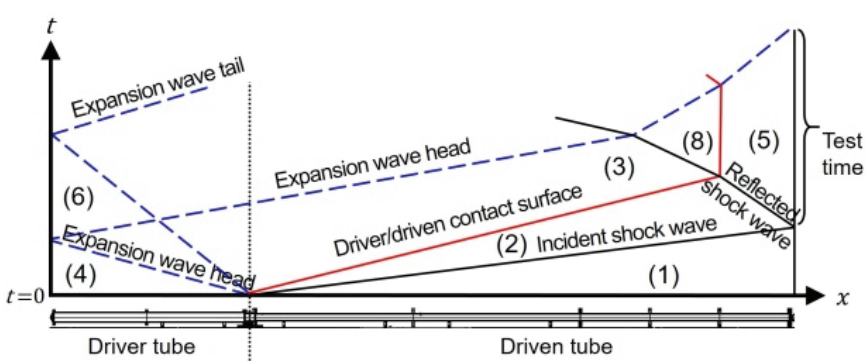

Fig. 1. x-t diagram for a conventional shock tube.

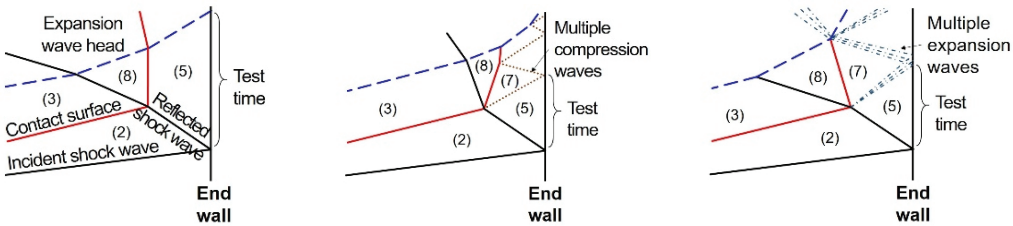

(a) Tailored condition (b) Over-tailored condition (c) Under-tailored condition

Fig. 2. Three different contact surface/reflected shock wave interactions.

achieve the tailoring conditions without affecting the test flow condition. This is known as driver gas tailoring [20, 21,24,25].

Expansion waves were generated at the same time as the incident shock wave generation and propagated to the driver tube end wall and reflected. The arrival of the reflected expansion waves from the driver tube end wall to the test flow caused gradual decreases in the test flow pressure and terminates the test time. The arrival of the expansion waves is generally slower than the contact surface/reflected shock wave interactions. Therefore, the test time can be extended by satisfying the tailoring conditions. If the driven tube is very long compared to the driver tube, the driver tube may be extended to delay the arrival of the expansion waves [16].

2.2 Theoretical Modeling

The driver gas compositions were adjusted to apply the driver gas tailoring technique because controlling the initial temperature of the driver or test gases was complex [27]. The modeling process for calculating the tailored driver gas composition is as follows.

The shock tube flow was assumed to be a one-dimensional adiabatic flow. All gases were assumed to be non-reacting cold gases. The viscous effects and heat transfer on the shock tube wall were not considered. For a simple ideal calculation, the mixing across the contact surface was ignored. The modeling was for calculating the tailored driver gas composition; the test gas conditions were not considered controllable variables. For a simple and ideal shock tube flow with the abovementioned assumptions, the following expressions for the contact surface tailoring condition could be derived by matching the pressure between the flow behind the reflected shock wave and the flow behind contact surface after the interaction [28]:

$$\frac{v_2}{a_3} = \frac{(\alpha_4-1)\left(\left(\frac{P_5}{P_2}\right)-1\right)}{\sqrt{(\alpha_4+1)\left(a_4\left(\frac{P_5}{P_2}\right)+1\right)}} \quad (1)$$

where, α is defined as $\alpha = \frac{\gamma+1}{\gamma-1}$. The pressure ratio between the flow behind the reflected shock wave and the flow behind the incident shock wave can be obtained from the well-known Rankine-Hugoniot equation [29].

$$\frac{P_5}{P_2} = \frac{2\gamma_1 M_R^2-(\gamma_1-1)}{\gamma_1+1} = \frac{M_S^2(3\gamma_1-1)-2(\gamma_1-1)}{M_S^2(\gamma_1-1)+2} \quad (2)$$

The flow pressure and the particle velocities across the contact surface were the same because the mixing effect was ignored ($P_2 = P_3$, and $v_2 = v_3$). Eq. 3, which has a unique solution, is a modified tailoring equation with the incident shock wave Mach number and the averaged specific heat ratio of the driver gas as variables (rearranging Eq. 1 ignoring the mixing effect through the contact surface).

$$M_{3,Tailored} = \frac{v_3}{a_3} = \frac{(\alpha_4-1)\left(\left(\frac{P_5}{P_2}\right)-1\right)}{\sqrt{(\alpha_4+1)\left(a_4\left(\frac{P_5}{P_2}\right)+1\right)}} = f(\gamma_4, M_S) \quad (3)$$

The tailored Mach number of the flow behind the contact surface ($M_{3,Tailored}$) could be matched by adjusting the averaged specific heat ratio of the driver gas.

The above equation lacks information on the tailored driver gas composition and the shock tube filling conditions, which is necessary to perform the actual experiment. Thus, the shock tube flow modeling was performed to obtain substantive information. Fig. 3 represents the flow behavior inside the shock tube with a uniform diameter.

The stagnant driver gas (in condition (4)) expanded and accelerated through the expansion waves to the flow condition (3). The flow with an oblique pattern represents the driver gas, while that with a checkered pattern represents the test gas. The flow expansion through the expansion waves assumed to be an unsteady isentropic process. When the Riemann variable was applied to the unsteady isentropic process, the following equation was satisfied between the flow conditions before and after the expansion [29].

$$\left(\frac{2}{\gamma_4-1}\right)a_4 = \left(\frac{2}{\gamma_4-1}\right)a_3 + v_3 \tag{4}$$

The particle velocities across the contact surface were assumed to be the same because the mass diffusion through the contact surface was ignored. Meanwhile, the particle velocity behind the incident shock wave can be obtained from the Rankine-Hugoniot equations of the shock wave fixed coordinates [29]. Eq. 5 represents the Mach number of the flow behind the contact surface with the incident shock wave Mach number as the variable (rearranging Eq. 4 using the Rankine-Hugoniot equation).

$$M_3 = \frac{v_2}{a_3} = \frac{\frac{2a_1}{\gamma_1+1}\left(M_S-\frac{1}{M_S}\right)}{\left(a_4-\frac{\gamma_4-1}{2}\left(\frac{2a_1}{\gamma_1+1}\left(M_S-\frac{1}{M_S}\right)\right)\right)} = f(\gamma_4, M_S) \tag{5}$$

The averaged molecular weight and the specific heat ratio of the driver gas can be expressed by mole fractions. The mixed driver gases with two different species were considered for simplicity. When specifying the two gases composing the driver gas, only one variable, X_b, is present in the following expression [24].

Fig. 3. Flow development inside a shock tube.

$$\begin{cases} \mathcal{M}_4 = \sum_i X_i\mathcal{M}_i = X_b + (1-X_b)\mathcal{M}_m = f(X_b) \\ \gamma_4 = \sum_i \left[\frac{X_i\mathcal{M}_i C_{P,i}}{X_i\mathcal{M}_i C_{V,i}}\right] = \frac{X_b\mathcal{M}_b C_{P,b} + (1-X_b)\mathcal{M}_m C_{P,m}}{X_b\mathcal{M}_b C_{V,b} + (1-X_b)\mathcal{M}_m C_{V,m}} = f(X_b) \end{cases} \tag{6}$$

The tailored driver gas composition calculation was performed as follows based on Eqs. 3 and 5:

(i) Calculate the incident shock wave Mach number (M_S) to generate the target test flow condition.

(ii) Specify the two gases of the driver gas: one is a base gas of the driver gas and the other is for mixing.

(iii) Solve $M_3 = M_{3,Tailored}$ for the mole fraction of the base gas (X_b).

The specific heat ratio and the molecular weight of the driver gas changed; hence, the driver tube filling pressure should also be recalculated. The pressure ratio across the incident shock wave P_2/P_1 can be obtained using the Rankine-Hugoniot equations. P_3/P_2 is one because the mixture effect and the mass diffusion across the contact surface were ignored. The pressure ratio before and after the unsteady isentropic expansion (P_4/P_3) can be obtained using the adiabatic gas law and the Riemann variable [30]. Therefore, the filling pressure ratio between the driver and the driven tubes (P_4/P_1)can be obtained as follows [29]:

$$\frac{P_4}{P_1} = \frac{P_2}{P_1}\frac{P_3}{P_2}\frac{P_4}{P_3} = \left(\frac{2\gamma_1 M_S^2 - (\gamma_1-1)}{\gamma_1+1}\right)\left(1-\frac{\gamma_4-1}{\gamma_1+1}\frac{a_1}{a_4}\left(M_S-\frac{1}{M_S}\right)\right)^{-\frac{2\gamma_4}{\gamma_4-1}} = f(M_S, X_b) \tag{7}$$

2.3 Experimental Details

The experiments were conducted in the K1 shock tunnel (Table 1), which was composed of a shock tube, a nozzle, and a test section. Fig. 4 shows the schematic of the test facility. The shock tube was composed of a 2.4 m-long

driver tube, a 0.06 m-long transition section, and a 3.6 m-long driven tube with inner diameters 68, 68, and 47.5 mm, respectively. The diaphragms were placed between each of the parts to separate them physically. The transition section was a component that induced the diaphragm rupture at the desired timing. The facility operation was initiated when the high-pressurized gas in the transition section was vented outside using a high-speed solenoid valve. The diaphragms then ruptured because of the high-pressure difference, and the strong incident shock wave generated. The driver gas with a tailored composition was used to fill the driver tube, while high-purity helium (99.9%) was used to fill the transition section. Dry air filled the driven tube as a test gas. The test gas expanded through a nominal Mach 6 conical nozzle.

One flow condition was considered. Table 2 summarizes the steady flow properties at the shock tube end wall and the nozzle exit. The physical quantities of the table are expressed with three significant figures. The steady flow properties at the shock tube end wall were determined using the Rankine-Hugoniot equations with the incident shock wave Mach number as the input. Using the Mach number according to the nozzle exit-to-throat area ratio, the steady flow properties at the nozzle exit were calculated using the isentropic expansion relations. The nozzle exit pitot pressure (P_{pt}) was calculated using the well-known Rayleigh pitot relation [29].

Table 2. Calculated test flow condition.

Location	Property	Value
Shock Tube End Wall	M_S [-]	3.3
	P_0 [MPa]	2.69
	T_0 [K]	1620
	ρ_0 [kg/m^3]	5.77
	h_0 [MJ/kg]	1.57
Nozzle Exit	M_∞ [-]	6.06
	P_∞ [kPa]	1.60
	T_∞ [K]	195
	ρ_∞ [kg/m^3]	0.03
	P_{pt} [kPa]	76.4

The flow pressure behind the reflected shock wave (regarded as the end wall pressure P_0) and the nozzle exit pitot pressure (P_{pt}) were measured using a flush-mounted piezoelectric pressure transducer. It is to be noted that the flow pressure behind the reflected shock wave was measured 45.5 mm upstream of the shock tube end wall. The incident shock wave propagation speed was monitored using two flush-mounted pressure transducers. One was the abovementioned near-end wall pressure transducer. The other was located at the shock tube wall, which was 68.5 mm upstream of the end wall. The shock tube considered herein was a convergent shock tube whose driver tube diameter was larger than that of the driven tube. The shock tube modeling for the convergent shock tube should be modified because additional flow accelerations can occur where the cross-sectional area changes [25]. However, previous research results involving the present shock tube indicated that the flow behavior inside the shock tube was similar to that of the shock tube with a uniform diameter [4,7,9,11,31,32]. Furthermore, the converging ratio of the present shock tube was relatively small. Therefore, the shock tube modeling was performed with a constant cross-sectional area and compared with the

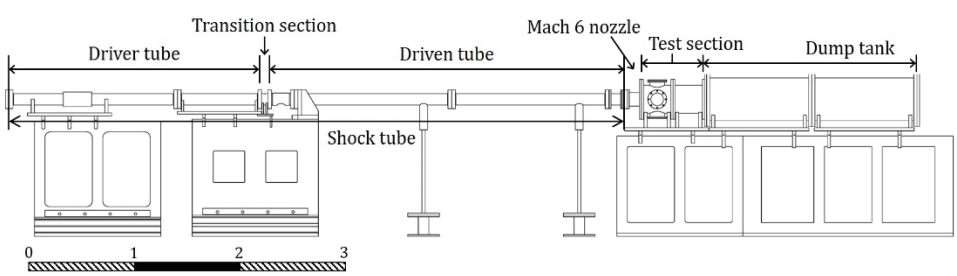

Fig. 4. Schematic of test facility.

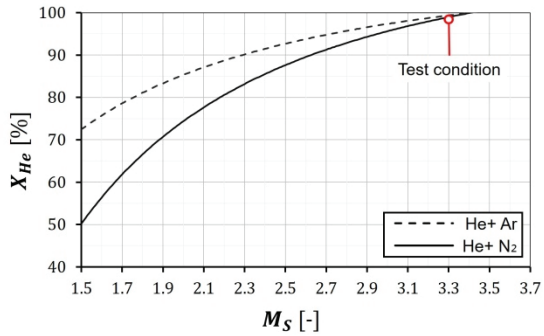

Fig. 5. Tailored driver gas composition curves.

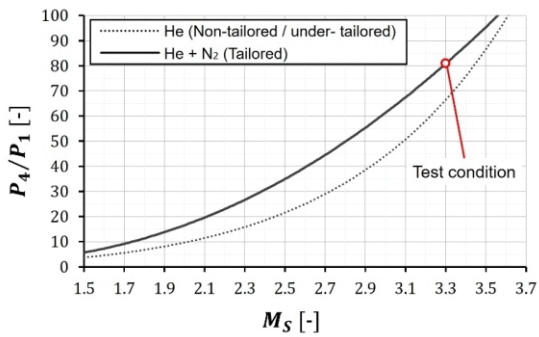

Fig. 6. Diaphragm bursting pressure ratio curves.

experimental results.

3. Results and Discussion

3.1 Modeling Results

The calculations from the previous section were implemented through a MATLAB code, which calculated the tailored driver gas composition with the initial gas temperature and the incident shock wave Mach number as the inputs. Helium was selected as the base gas, while the gases with larger molecular weights were considered to the mixing gas. The initial temperature of the driver and test gases was assumed to be 290 K. Fig. 5 shows the tailored driver gas composition curves of the helium-nitrogen and helium-argon mixture. The helium mole fractions in the driver gas for the tailoring condition according to the incident shock wave Mach number are represented. The considered incident shock wave Mach number was from 1.50 to 3.66, which corresponded to the test flow total temperature ranges from 487 K to 1955 K.

The higher the incident shock wave Mach number, the higher the helium mole fraction was required (Fig. 5). Helium was a suitable base gas for the tailoring conditions with a higher incident Mach number, while nitrogen or argon was efficient as a base gas for the tailoring conditions with a lower incident Mach number. In both cases, if the incident shock wave Mach number exceeded 3.4, the mole fraction of helium would reach 100%. Helium alone driver gas could satisfy the tailoring conditions in the corresponding test conditions. Compared with the results of the helium-nitrogen mixture, the helium mole fraction of the helium-argon mixture was always high for the same incident shock wave Mach number. The molecular weight of argon is larger than that of nitrogen; hence even a small amount of argon causes a significant change in the driver gas properties.

The target incident shock wave Mach number was 3.3. The tailored helium mole fractions that satisfied the corresponding target condition were 98.97%, and 99.37% for the nitrogen and argon mixtures, respectively. These results are consistent with those obtained by Hong et al. [25]. As mentioned earlier, argon has a larger molecular weight. Thus, even a slight error in the driver gas composition can cause the failure of satisfying the tailoring conditions. Therefore, the driver gas tailoring was performed herein using a helium-nitrogen mixture.

Figure 6 represents the diaphragm bursting pressure ratio against the incident shock wave Mach number for the non-tailored and tailored conditions. The diaphragm bursting pressure ratio was identical to the filling pressure ratio between the driver and the driven tubes. In the figure, 'non-tailored' represents the calculated shock tube filling conditions using Eq. 7 without applying the driver gas tailoring calculation. The non-tailored driver gas was 100% helium, which indicates the under-tailored condition compared to Fig. 5. For the tailored driver gas, the driver tube filling pressure should be increased to recover the

Mach number of the incident shock wave because the average molecular weight of the driver gas increased. The ratio of the driver and driven tube filling pressures was calculated as approximately 70.3 for the target test condition.

3.2 Shock Tunnel Results

Table 3 presents the tested shock tube filling conditions. Case A represents the under-tailored results with the 100% helium driver gas. Cases B and C denote the near-tailored conditions. The shock tunnel tests were each performed three times, and the uncertainty was examined based on these shots.

Table 3. Shock tube filling conditions.

Location	Property	Tested Case		
		Case A	Case B	Case C
Driver Tube	P_4 [MPa]	2.80	3.15	3.25
	T_4 [K]	290	290	290
	Filling gas	He	He-N2	He-N2
	X_{He} [%]	100	98.0	97.5
	γ_4 [-]	1.67	1.66	1.65
	$\mathcal{M}_4$ [kg/mol]	0.00400	0.00448	0.00460
Driven Tube	P_1 [MPa]	0.04		
	T_1 [K]	290		
	Filling gas	Dry air		
	γ_1 [-]	1.40		
	$\mathcal{M}_1$ [kg/mol]	0.0289		

Table 4. Incident shock wave Mach number comparison.

	Target (calculated)	Case A (non-tailored/ under-tailored)	Case B (near-tailored)	Case C (near-tailored)
v_S [m/s]	1126	1150 ±15	1167 ±20	1142 ±13
M_S [-]	3.3	3.37 ±0.05	3.42 ±0.06	3.34 ±0.04
ε_{M_S} [%]	-	+2.0	+4.8	+1.3

Table 4 shows the comparisons of the velocities and the Mach numbers of the incident shock wave for each case. The incident shock wave velocity and the Mach number were directly related to the test flow condition and should be checked. The measured velocities and the Mach numbers of the incident shock wave were found to agree well within a margin of error. The "±" symbol in the table indicates a 95% confidence level for each of the properties based on multiple shots.

The effects of the tailored driver gas composition were examined from the time histories of the pressure measurements behind the reflected shock wave (Fig. 7). Time (t) in the figure represents the measured time of the

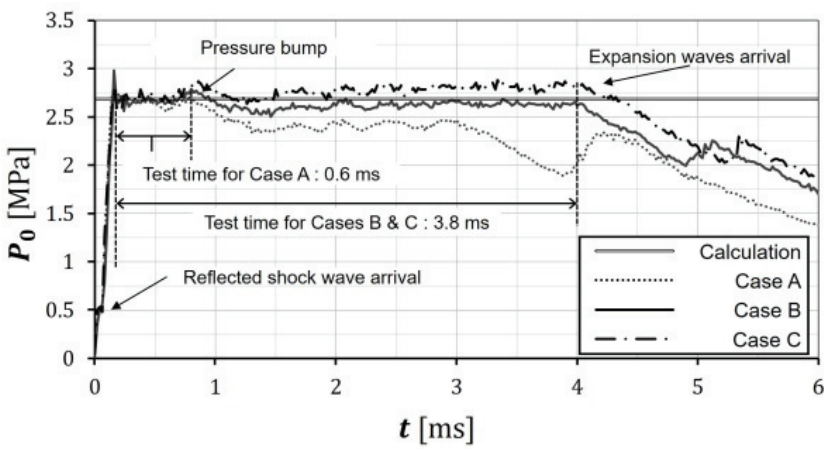

Fig. 7. Pressure histories behind the reflected shock wave.

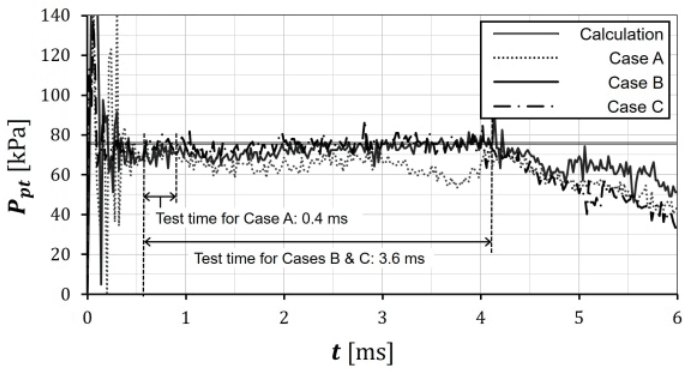

Fig. 8. Nozzle exit pitot pressure histories.

flow arrival at the pressure transducers. Looking at the pressure data before 0.5 ms, the high-pressure flow, which was the test flow, was formed as soon as the reflected shock wave arrived at the end wall, and the same level of total pressures was developed regardless of the driver gas compositions. For all cases, a weak pressure bump was observed near 0.75 ms. This pressure bump was thought to have originated from the mixing layer generation of the driver and test gases [33] and the bifurcation of the reflected shock wave near the end wall [34]. After the pressure bump, the pressure behavior appeared differently depending on the driver gas compositions. The pressure for the under-tailored condition (Case A) decreased. Regarding the two near-tailored conditions (cases B and C), near-uniform pressure behaviors were observed until approximately 4 ms. Comparing the pressure histories after 1.2 ms, a small pressure decrease was observed for Case B, while an increase occurred Case C. However, in both cases, the differences between the pressure value before the pressure bump (to 0.8 ms) and that after the pressure bump (from 1.1 ms to 4.0 ms) were within 5%. Therefore, these two conditions were thought to be in near-tailored conditions. For the near-tailored conditions, the uniform pressure behaviors were terminated by the arrival of the expansion waves reflected at the driver tube end wall. Compared with the under-tailored condition, the arrival of the expansion waves was delayed for the near-tailored conditions. The propagation speed of the expansion waves depends on the acoustic speed of the medium. The tailored driver gas had a larger molecular weight than helium and a lower acoustic speed; therefore, the arrival of the expansion waves was delayed.

Figure 8 represents the results of the nozzle exit pitot pressure measurements. The test time began after the nozzle flow establishment for 0.6 ms. The under-tailored case provided only 0.4 ms of test time. Unlike in Fig. 7, the pitot pressure behaviors for the near-tailored conditions were similar. The flow expansion through the nozzle was thought to reduce the pressure difference found in the shock tube end wall flow. The nozzle exit flow can be interpreted as more obtuse to the change in the driver gas composition and the initial filling pressure of the driver tube than the shock tube end wall flow. As a result, the test time was extended to 3.6 ms after the driver gas tailoring application.

Table 5 shows the comparison results of the average and calculated values during the test time for each case. The numbers in parentheses indicate 95% confidence levels for each of the measured pressures during steady flow. The test times in the table indicate the steady flow period of the nozzle exit flow. Compared with the calculated values, the flow properties during the test time agreed well within a margin of error around 7%, indicating a successful driver gas tailoring application.

Table 5. Comparison of steady flow properties.

	Calculated	Case A (non-tailored/ under-tailored)	Case B (near-tailored)	Case C (near-tailored)
P_0 [MPa]	2.69	2.66(±0.017)	2.63(±0.007)	2.77 (±0.008)
ε_{P_0} [%]	-	-0.9	-2.1	+2.9
P_{pt} [kPa]	76.4	71.3 (±1.98)	72.7 (±0.54)	75.0 (±0.50)
$\varepsilon_{P_{pt}}$ [%]	-	-7.1	-5.2	+2.2
Test Time [ms]	-	0.4	3.6	3.6

4. Conclusions

The driver gas tailoring technique was used to extend the K1 shock tunnel test time, which controls the behavior of the contact surface. The target incident shock wave Mach number and the stagnation temperature were 3.3 and 1623 K, respectively. The tailored compositions of conventional driver gases (i.e., He-N_2 and He-Ar gas mixtures) were calculated through uniform-diameter shock tube flow modeling. As a result of modeling, the He-N_2 mixture was expected to reduce the composition error compared to the He-Ar mixture, therefore used as the driver gas in the shock tunnel experiments. The incident shock wave Mach number, flow pressure behind the reflected shock wave near the shock tube end wall, and pitot pressure at the nozzle exit were measured to examine the effect of driver gas tailoring. The pressure decreased because of the contact surface/reflected shock wave interactions observed in the under-tailored case. Meanwhile, the results of the near-tailored conditions presented uniform pressure histories after the pressure bump. The shock tunnel test time was extended to approximately 3.6 ms, where the under-tailored test time was about 0.4 ms.

Acknowledgements

This work was supported by the Scramjet Combined Propulsion System Project (No.16-106-501-035) of Republic of Korea.

References

1. Bertin, J. J., "Hypersonic Aerothermodynamics," Vol. 1, p. 160, 3rd ed., The American Institute of Aeronautics and Astronautics, Washington, DC, 1994.
2. Park, G., "Oxygen Catalytic Recombination on Copper Oxide in Tertiary Gas Mixtures," Journal of Spacecraft and Rockets, Vol. 50, No. 3, 2013, pp. 540–555.
3. Cheung, T. M., Schrijer, F. F. J., and Park, G., "Nitrogen Catalytic Recombination on Copper Oxide in Tertiary Gas Mixtures," Journal of Spacecraft and Rockets, Vol. 53, No. 4, 2016, pp. 644–653.
4. Jo, S. M., Shim, H., Park, G., Kwon, O. J., and Kim, J. G., "Temperature Determination in a Shock Tube Using Hydroxyl Radical A-X Band Emission," Physics of Fluids, Vol. 31, No. 2, 2019, 026109.
5. Kim, I., Park, G., and Na, J. J, "Experimental Study of Surface Roughness Effect on Oxygen Catalytic Recombination," International Journal of Heat and Mass Transfer, Vol. 138, 2019, pp. 916–922.
6. Kim, I., and Park, G., "Experimental Study of Oxygen Catalytic Recombination on a Smooth Surface in a Shock Tube," Applied Thermal Engineering, Vol. 156, 2019, pp. 678–691.
7. Yang, Y., Kim, I., and Park, G., "Experimental and Numerical Study of Oxygen Catalytic Recombination of SiC-Coated Material," International Journal of Heat and Mass Transfer, Vol. 143, 2019, 118510.
8. Kim, I., Lee, S., Kim, J. G., and Park, G., "Analysis of Nitrogen Recombination Activity on Silicon Dioxide with Stagnation Heat-Transfer," Acta

Astronautica, Vol. 177, 2020, pp. 386–397.
9. Kim, I., Lee, S., Park, G., and Lee, J. K., "Overview of Flow Diagnosis in a Shock Tunnel," International Journal of Aeronautical and Space Sciences, Vol. 18, No. 3, 2017, pp. 425–435.
10. Lee, S., Oh, B.-S, Kim, Y., and Park, G., "High-Altitude Environment Simulation of Space Launch Vehicle in a Ground-Test Facility," Journal of the Korean Society for Aeronautical and Space Sciences, Vol. 45, No. 11, 2017, pp. 914–921.
11. Lee, S., Song, H., Park, G., and Lee, J. K., "Freefalling Heated Sphere in a Shock Tunnel," AIAA Journal, Vol. 55, No. 11, 2017, pp. 3995–3998.
12. Park, G., Park, C., Jin, Y., Choi, H., Byun, J., and Hwang, K., "Ethylene Transverse Jets in Supersonic Crossflows," Journal of Propulsion and Power, Vol. 31, No. 3, 2015, pp. 773–788.
13. Chang, W. K, Park, G., Jin, Y., and Byun, J., "Shock Impinging Effect on Ethylene Flameholding," Journal of Propulsion and Power, Vol. 32, No. 5, 2016, pp. 1230–1239.
14. Chang, E. W. K., Yang, S., Park, G., and Choi, H., "Ethylene Flame-Holding in Double Ramp Flows," Aerospace Science and Technology, Vol. 80, 2018, pp. 413–423.
15. Kim, K., Park, G., and Jin, S., "Flameholding Characteristics of Ethylene-Fueled Model Scramjet in Shock Tunnel," Acta Astronautica, Vol. 161, 2019, pp. 446–464.
16. Yang, S., Kim, K., Chang, E. W. K., Jin, S., and Park, G., "Scramjet Experimental Techniques Using a Shock Tunnel," Journal of the Korean Society of Propulsion Engineers, Vol. 22, No. 5, 2018, pp. 97–106.
17. Rudinger, G., "Effect of Boundary-Layer Growth in a Shock Tube on Shock Reflection from a Closed End," Physics of Fluids, Vol. 4, No. 12, 1961, pp. 1463–1473.
18. Petersen, E. L., and Hanson, R. K., "Nonideal Effects Behind Reflected Shock Waves in a High-Pressure Shock Tube," Shock Waves, Vol. 10, No. 6, 2001, pp. 405–420.
19. Hooker, W. J., "Testing Time and Contact-Zone Phenomena in Shock-Tube Flows," Physics of Fluids, Vol. 4, No. 12, 1961, pp. 1451–1463.
20. Campbell, M. F., Wang, S., Goldenstein, C. S., Spearrin, R. M., Tulgestke, A. M., Zaczek, L. T., Davidson, D. F., and Hanson, R. K., "Constrained Reaction Volume Shock Tube Study of n-Heptane Oxidation: Ignition Delay Times and Time-Histories of Multiple Species and Temperature," Proceedings of the Combustion Institute, Vol. 35, No. 1, 2015, pp. 231–239.
21. Campbell, M. F, Parise, T., Tulgestke, A. M., Spearrin, R. M., Davidson, D. F., and Hanson, R. K., "Strategies for Obtaining Long Constant-Pressure Test Times in Shock Tubes," Shock Waves, Vol. 25, No. 6, 2015, pp. 651–665.
22. Trass, O., and Mackay, D., "Contact Surface Tailoring in a Chemical Shock Tube," AIAA Journal, Vol. 1, No. 9, 1963, pp. 2161–2163.
23. Reddy, N. M., "An Analytic Method for Real Gas Tailoring in a Shock Tube," AIAA Journal, Vol. 9, No. 12, 1971, pp. 2458–2460.
24. Amadio, A. R., Crofton, M. W., and Petersen E. L., "Test-Time Extension Behind Reflected Shock Waves Using CO_2-He and C_3H_8-He Driver Mixtures," Shock Waves, Vol. 16, No. 2, 2006, pp. 157–165.
25. Hong, Z., Davidson, D. F., and Hanson, R. K., "Contact Surface Tailoring Condition for Shock Tubes with Different Driver and Driven Section Diameters," Shock Waves, Vol. 19, No. 4, 2009, pp. 331–336.
26. Brabbs, T. A., and Belles, F. E., "Contact-Surface Tailoring in Real Shock Tubes," NASA TN D-3043, October 1965.
27. Resler, E. L., Lin, S.-C, and Kantrowitz, A., "The Production of High Temperature Gases in Shock Tubes," Journal of Applied Physics, Vol. 23, No. 12, 1952, pp. 1390–1399.

28. Nishida, M., “Experimental Measurements of Hypersonic Flows,” Shock Tubes: Handbook of Shock Waves, Vol. 1, pp. 553-585. 1st ed., Academic Press, New York, 2001.
29. Oosthuizen, P. H., and Carscallen, W. E., “Introduction to Compressible Fluid Flow,” Vol. 1, pp. 94-115, pp. 151–201, 2nd ed., CRC Press Taylor & Francis Group, Boca Raton, FL, 2013.
30. Glass, I. I., and Sislian, J. P., “Nonstationary Flows and Shock Waves,” Vol. 1, pp.19–23, 1st ed., Oxford University Press, Walton Street, 1964.
31. Song, H., Lee, S., Lee, J. K., and Park, G., “Attitude Angle and Drag Coefficient Measurements of Free-Falling Hemisphere Using a Visualization Technique,” Journal of the Korean Society for Aeronautical and Space Sciences, Vol. 45, No. 8, 2017, pp.619–626.
32. Park, S.-H., and Park, G., “Separation Process of Multi-Spheres in Hypersonic Flow,” Advances in Space Research, Vol. 65, No. 1, 2020, pp. 392–406.
33. Polachek, H., and Seegar, R. J., “On Shock-Wave Phenomena; Refraction of Shock Waves at a Gaseous Interface,” Physical Review, Vol. 84, No. 5, 1951, pp. 922–929.
34. Weber, Y. S., Oran, E. S., Boris, J. P., and Anderson, J. D., “The Numerical Simulation of Shock Bifurcation Near the End Wall of a Shock Tube,” Physics of Fluids, Vol. 7, No. 10, 1995, pp. 2475–2488.